The Astrophysical Journal, 891:89 (8pp), 2020 March 1 https://doi.org/10.3847/1538-4357/ab7005

The Frequency Drift and Fine Structures of Solar S-bursts in the High Frequency Band of LOFAR

PeiJin Zhang[1,2,3], Pietro Zucca[3], ChuanBing Wang[1,2,4], Mario M. Bisi[5], Bartosz Dąbrowski[6], Richard A. Fallows[3], Andrzej Krankowski[6], Jasmina Magdalenic[7], Gottfried Mann[8], Diana E. Morosan[9], and Christian Vocks[8]
[1] CAS Key Laboratory of Geospace Environment, School of Earth and Space Sciences, University of Science and Technology of China, Hefei, Anhui 230026, People's Republic of China
[2] CAS Center for the Excellence in Comparative Planetology, Hefei, Anhui 230026, People's Republic of China
[3] ASTRON, The Netherlands Institute for Radio Astronomy, Oude Hoogeveensedijk 4, 7991 PD Dwingeloo, The Netherlands; zucca@astron.nl
[4] Mengcheng National Geophysical Observatory, Hefei, Anhui 230026, People's Republic of China
[5] RAL Space, United Kingdom Research and Innovation (UKRI)—Science and Technology Facilities Council (STFC)—Rutherford Appleton Laboratory (RAL), Harwell Campus, Oxfordshire, OX11 0QX, UK
[6] Space Radio-Diagnostics Research Centre, University of Warmia and Mazury in Olsztyn, Olsztyn, Poland
[7] Solar-Terrestrial Centre of Excellence, SIDC, Royal Observatory of Belgium, B-1180 Brussels, Belgium
[8] Leibniz-Institut für Astrophysik Potsdam (AIP), An der Sternwarte 16, D-14482 Potsdam, Germany
[9] Department of Physics, University of Helsinki, P.O. Box 64, FI-00014 Helsinki, Finland
Received 2019 September 3; revised 2020 January 23; accepted 2020 January 23; published 2020 March 6

Abstract

Solar S-bursts are short duration (<1 s at decameter wavelengths) radio bursts that have been observed during periods of moderate solar activity, where S stands for short. The frequency drift of S-bursts can reflect the coronal density variation and the motion state of the electron beams. In this work, we investigate the frequency drift and the fine structure of the S-bursts with the Low Frequency Array (LOFAR). We find that the average frequency drift rate of the S-bursts within 20–180 MHz could be described by $df/dt = -0.0077f^{1.59}$, combined with previous results in low frequency. With the high time and frequency resolution of LOFAR, we can resolve the fine structures of the observed solar S-bursts. A fine drift variation pattern was found in the structure of S-bursts (referred to as solar Sb-bursts in this paper) during the type-III storm on 2019 April 13, in the frequency band of 120–240 MHz. The Sb-bursts have a quasiperiodic segmented pattern, and the relative flux intensity tends to be large when the frequency drift rate is relatively large. This kind of structure exists in about 20% of the solar S-burst events within the observed frequency range. We propose that the fine structure is due to the density fluctuations of the background coronal density. We performed a simulation based on this theory that can reproduce the shape and relative flux intensity of the Sb-bursts. This work shows that the fine structure of solar radio bursts can be used to diagnose the coronal plasma.

Unified Astronomy Thesaurus concepts: Solar radio emission (1522); Solar corona (1483); Radio bursts (1339); Radiative transfer (1335)

1. Introduction

Solar S-bursts are short duration radio bursts with narrow bandwidths. They were first identified by Ellis (1969) as a new type of short duration radio burst, and named "fast drift storm bursts." Later, McConnell (1982) carried out a statistical study of these "fast drift storm bursts" and renamed them solar S-bursts as they showed similar characteristics to Jovian S-bursts. The statistical results (McConnell 1982; Melnik et al. 2010; Morosan et al. 2015; Morosan & Gallagher 2017; Clarke et al. 2019) showed that the FWHM duration of the S-burst is about 50 ms at a given frequency, the instantaneous bandwidth is about 120 kHz. Solar S-bursts always occur superimposed on a background of other solar radio activity, such as type IIIs, type IIIbs, and spikes. The frequency drift rate of S-bursts is generally about 1/3 to 1/2 of the accompanying type III bursts. It is also found that the instantaneous frequency width of solar S-bursts increases linearly with frequency (Melnik et al. 2010; Clarke et al. 2019). Melrose (1982) argued that solar S-bursts are a similar phenomenon to the drift pair bursts with reflections. A recent observation of drift pairs bursts indicates that the drift pairs have almost the same frequency drift rate as the S-bursts (Stanislavsky et al. 2017). McConnell & Ellis (1981) identified the fringed structure in type-S bursts, which was reported to exist in 1% of the type-S events in the frequency band of 30–82 MHz. The fringed structure is regularly spaced at about 100 kHz between the bright stripes. The single elements of the fringes have narrow bandwidth down to 10–15 kHz (McConnell 1982, 1983). So far, there have been very few studies on the fine structure of solar S-bursts because of the limited sensitivity and resolution of previous observations.

The Low Frequency Array (LOFAR) is an advanced radio antenna array (van Haarlem et al. 2013). It has two types of arrays observing in two frequency bands, the Low Band Array in the frequency range of 10–90 MHz and the High Band Array (HBA) in the frequency range of 110–250 MHz. LOFAR has 51 stations, 38 of them located in the northeast of the Netherlands, and 13 international stations located in Germany, Poland, France, Sweden, Ireland, and the UK. LOFAR is capable of a variety of processing operations including correlation for standard interferometric imaging and the tied-array beam-forming. With the high time and frequency resolution of LOFAR observations, we can resolve the fine structure of solar S-bursts.

The emission mechanism of S-bursts is still an open question. Several mechanisms could be used for the interpretation of S-bursts. For example the electron cyclotron maser (ECM) emission was first proposed by Wu & Lee (1979) for the auroral kilometric radiation of the Earth, and was used to

interpret the fine structure of solar type III radio bursts (the type IIIb burst) (Wang 2015). The ECM emission is generated in the condition of $f_{ce}/f_{pe} > 1$, where f_{ce} is the electron cyclotron frequency and f_{pe} is the local plasma frequency. The condition of $f_{ce}/f_{pe} > 1$ requires tenuous plasma and relatively strong magnetic fields. Melnik et al. (2010) proposed a model for S-bursts, in which the electromagnetic wave is generated in the processes of the coalescence of fast magnetosonic waves with Langmuir waves. According to a recent study by Morosan et al. (2016), the most likely emission mechanism for meter/decameter frequency radio bursts is plasma emission, since the magnetic field at the height of these radio bursts is not high enough to produce ECM emission. However, Kolotkov et al. (2018) argued that the magnetic field would be sufficient to excite ECM emission when there is enough complexity in the magnetic field configuration. In addition, the condition of the ECM can be satisfied with the assumption of density-depleted magnetic flux tubes (Wu et al. 2002; Wang 2015). Based on this assumption, the true source region, where the radio wave is generated by ECM, is inside the tube, and the wave cannot leave the tube until it arrives at an altitude where the local exterior cutoff frequency is equal to the wave frequency (the apparent source region). Which means, the apparent source of ECM emission also satisfies that the wave frequency is approximately equal to the local plasma frequency of the "observed source region." Although the emission mechanism of solar S-bursts is still debated, the observed emission originates in regions of local plasma frequency levels (McConnell 1983; Melnik et al. 2010; Morosan et al. 2015). Thus, we assume that S-bursts are generated close to the plasma frequency.

The coronal plasma has various length scales of density fluctuations from up to a few solar radii down to kilometer scales (Woo 1996). The density fluctuations of the the corona plasma can result in the fine-structured solar radio bursts, and these fine structures can be used to study the density fluctuations of the corona. Kolotkov et al. (2018) used the quasiperiodic drifting fine structures of type III radio bursts to study the density variation caused by fast magnetoacoustic waves. Loi et al. (2014) used simulations to show that the fine structure in type III radio bursts could be due to the background density fluctuations. Mugundhan et al. (2017) and Chen et al. (2018) used the type IIIb radio bursts as a tracer to find that the spectrum of the density variation derived from the frequency gap between the striae fits well to the one-dimensional Kolmogorov spectral index (5/3) (Frisch & Kolmogorov 1995). Mann et al. (1989) used the perturbed density to interpret the fine structures in type IV radio bursts. In this work, we inspected the fine structure of S-bursts (referred to as Sb-bursts in the following), and demonstrated that the fine structure of Sb-bursts can be used to inspect the small scale (megameter) density fluctuations.

This paper is arranged as follows. In Section 2, we show observation results on the frequency drift rate of S-bursts from LOFAR HBA observations, the dynamic spectrum of six Sb-bursts, and the analysis of their characteristics. In Section 3, we qualitatively show that the relationship between the frequency drift rate and the relative flux intensity in the dynamic spectrum can be interpreted by Coulomb absorption of the wave with electron density fluctuations. Then, we show the simulation results that can reproduce the shape and relative flux intensity of the Sb-bursts. In Section 4 we present our conclusion and discussion.

2. S-burst Observations

In this study, we used dynamic spectra observations of the Sun obtained by a single HBA beam produced using the LOFAR core stations (van Haarlem et al. 2013). The synthesized beam that points at the solar center has a main lobe width (about $0.^{\circ}1$) smaller than the angular width of the Sun, which can help us avoid the emission from other directions and make sure the radio bursts originate from the Sun. The beam-formed observations provide a high-time and frequency resolution of 10.5 ms and 12.2 kHz. The observations were taken in the time interval from 05:40:00 UT to 17:39:59 UT on 2019 April 13. In this time interval we also observed a type III storm. An example of a dynamic spectrum during this time is shown in Figure 1. The S-burst shown in Figure 1(a) is a typical S-burst, while the S-burst in Figures 1(b) and (c) shows multilanes, similar to the "drift pair" bursts. The band-splitting width of the observed drift pair is about 0.5 MHz, the time difference between the lanes of the drift pairs is about 50 ms.

2.1. Frequency Drift Rate of S-bursts

We find 204 S-bursts during our 12 hr observation of the Sun. Figure 2 shows the dynamic spectrum of a typical S-burst in HBA, and its frequency drift rate and relative flux intensity. In the left subpanel of Figure 2, the blue line represents the center line of the S-burst, namely the frequency drift line. The frequency drift line is obtained using an iteration algorithm called ACBone (Zhang et al. 2018). This algorithm was used previously to statistically study the frequency drift rate of type III bursts. The code of ACBone is available online at Github. From the frequency drift line, we can obtain the frequency drift rate and the flux intensity of the S-burst at different frequencies, which is shown in the the right subpanel of Figure 2 with red and black curves, respectively. For the S-bursts shown in Figure 2 we can see that the frequency drift rate is stable near 12 MHz s^{-1}, corresponding to the smooth frequency drift line in the dynamic spectrum. The intensity shows a trend of increase and decrease at the first and second halves of this event.

For each event, we used a linear fit to the frequency drift line to get an average frequency drift rate (df/dt). The frequency drift rate of all S-bursts is shown in Figure 3, along with the previous results in low frequency. From Figure 3 we can see that the frequency drift rate of S-bursts agrees well with the fit of the low frequency observations (blue line in Figure 3). We fit the frequency drift line of these S-bursts in HBA to the power-law equation $df/dt = -af^b$, the fitting result is $df/dt = -0.0015f^{1.92}$. The combined fitting result of the S-bursts in HBA and the S-bursts in low frequency is $df/dt = -0.0077f^{1.59}$. The relation between the frequency and frequency drift rate is similar in the low frequency range (10–80 MHz) and the high frequency range (120–180 MHz), as shown in Figure 3.

2.2. Fine Structure of Sb-bursts

Out of these 204 events, we find that some of the S-bursts have a discontinuous structure. As examples, Figure 4 shows the dynamic spectrum, the frequency drift rate, and the relative flux intensity of six Sb-bursts with fine structures.

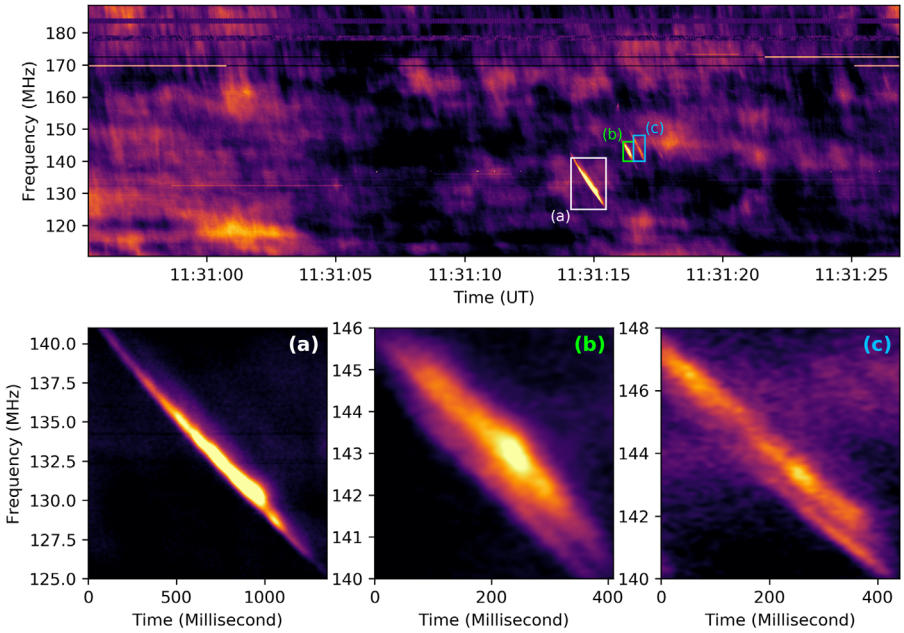

Figure 1. Example of the dynamic spectrum of HBA during the type-III storm on 2019 April 13. Three S-bursts are labeled as (a), (b), and (c) in the upper panel; the zoom-in views of these three S-bursts are shown in the lower panel.

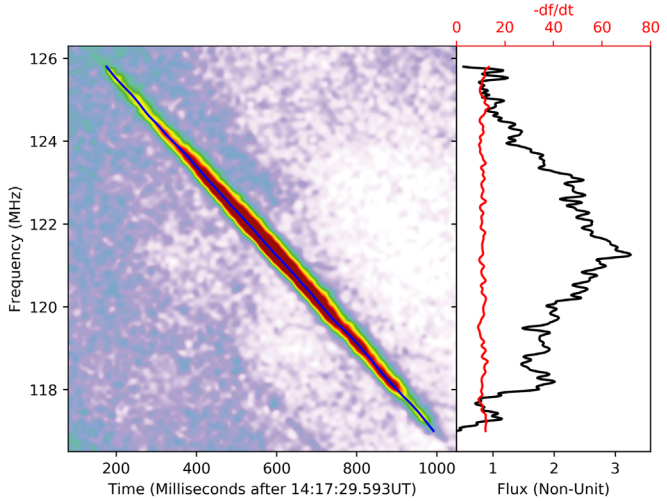

Figure 2. Dynamic spectrum shows an isolated S-burst. The right subpanel shows the frequency drift rate (red line) and the relative flux intensity of this S-burst (black line).

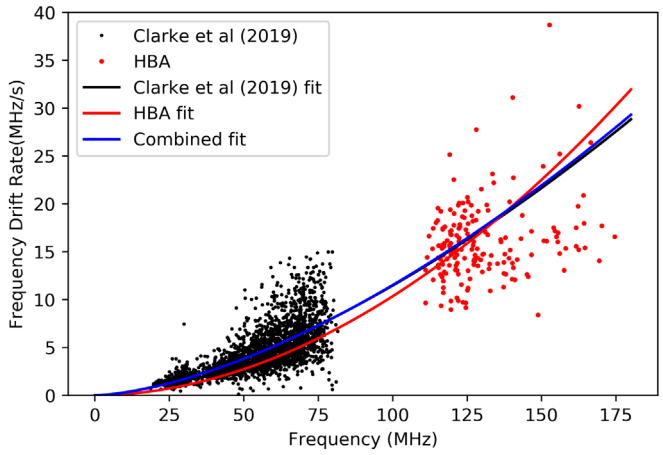

Figure 3. Frequency drift rate of S-bursts. The black points represent the previous results of the low frequency band of 20–70 MHz including observations from McConnell (1982), Dorovskyy et al. (2017), Morosan & Gallagher (2017), and Clarke et al. (2019). The red points mark the 204 events in the frequency range of 120–180 MHz on 2019 April 13. The red line shows the fitting result to the events in HBA ($df/dt = -0.0015f^{1.92}$), the black line shows the fitting result in low frequency ($df/dt = -0.0084f^{1.57}$), the blue line shows the combined fitting result of the S-bursts in HBA and low frequency ($df/dt = -0.0077f^{1.59}$).

Figure 4 shows an interesting pattern in the dynamic spectrum of the Sb-bursts. The Sb-bursts are segmented like chains, and the frequency drift line is relatively steeper near the local maximum of each segment. The frequency drift rate ($-df/dt$) and the the flux intensity ($I_{\rm obs}$) have a similar trend, namely the flux intensity tends to be large when the frequency drift rate is large. This trend can be seen in every left subpanel of Figure 4.

For these six events, we did a Pearson test and a linear fit between df/dt and $I_{\rm obs}$, and the results are shown in Figure 5 and Table 1. The Pearson correlation coefficient (CC) and the linear fit slope of these six selected events are all positive, which indicates a positive correlation between the frequency drift rate and the intensity. Among these six events, Event 6 has the largest correlation coefficient. The df/dt and $I_{\rm obs}$ of Events 1, 2, and 3 have significant correlation, Event 4 has moderate positive correlation, while Event 5 has weak correlation. In the following, we will propose a model to explain the positive correlation between the frequency drift rate and the flux intensity in the discontinuous structure of Sb-bursts.

3. Generation of the Fine Structure

In this section, we attempt to explain the shape and flux intensity in the fine structure of the Sb-burst by assuming the electron beams pass through a plasma with fluctuating background electron densities.

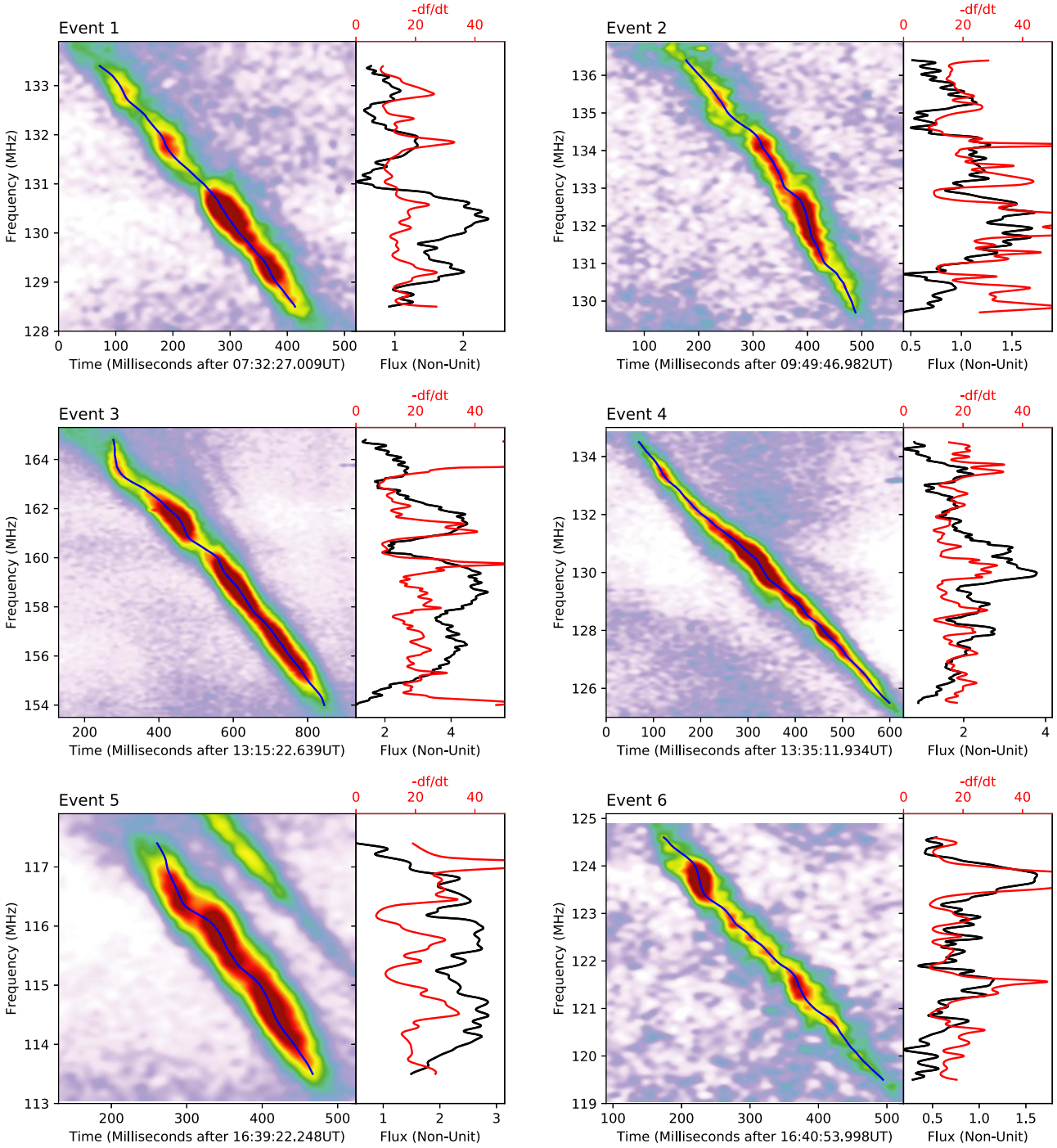

Figure 4. The dynamic spectrum, the frequency drift rate, and the relative flux intensity of six Sb-bursts with fine structures on 2019 April 13. In each panel, the left subpanel shows the dynamic spectrum with a frequency drift line, taken as the center line of the burst. The right subpanel shows the frequency drift rate (red line) and the relative flux intensity (black line) of the S-bursts. The left and right subpanels share the same *y*-axis.

3.1. The Relationship between Optical Depth and Frequency Drift Rate

When the electron beam is propagating outward at a speed of v_b, the frequency drift rate can be expressed as

$$\frac{df}{dt} = v_b \frac{df_{\rm pe}}{dh} \propto \frac{df_{\rm pe}}{dh}. \quad (1)$$

The frequency drift rate is proportional to the decreasing rate of the local plasma frequency with altitude. According to the plasma emission theory, the wave is generated near the plasma frequency $f_{\rm pe}$, which can be expressed by $f_{\rm pe}\,[\rm Hz] = 8.98 \times 10^3 \sqrt{N_{\rm e}[\rm cm^{-3}]}$. Here, N_e is the electron number density. Thus, the increasing and decreasing trends in the frequency drift rate in Figure 4 can be related directly to fluctuations in the background electron density.

The variation in the flux intensity can be interpreted by Coulomb collision absorption of the wave. The attenuation caused by collisional absorption is given by Benz (2012; p265,

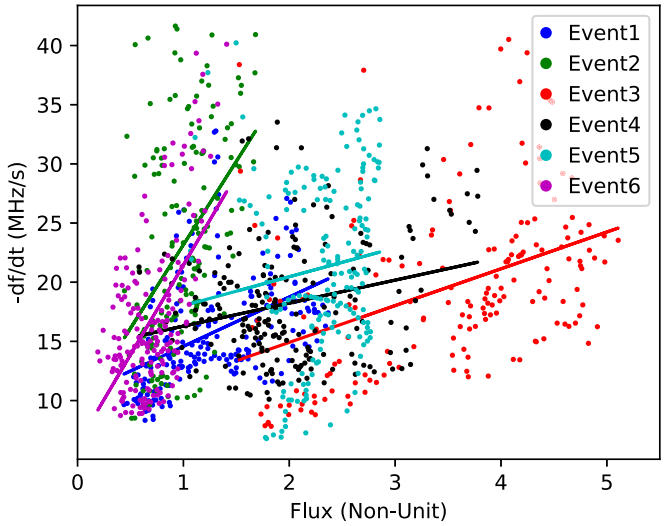

Figure 5. The linear fit of the frequency drift rate and flux intensity. Six colors mark the six events in Figure 4, the data points are obtained along the frequency drift line of each event, the solid line is the linear fit of the data points.

Table 1
The Pearson CC and Slope of the Linear Fit between $-df/dt$ and $I_{\rm obs}$

	Pearson CC	Slope
Event 1	0.44	4.16
Event 2	0.45	14.10
Event 3	0.42	3.11
Event 4	0.25	1.94
Event 5	0.12	2.44
Event 6	0.56	15.17

Equation 11.2.2):

$$I_{\rm obs} = I_0 e^{-\tau_c} \tag{2}$$

$$\tau_c = \int_{s_0}^{\rm inf} \kappa(s) ds$$

$$\kappa(s) \approx 9.88 \times 10^{-3} \frac{N_e \sum_i Z_i^2 N_i \ln\Lambda_t}{f_s^2 T^{3/2} \mu_r} [{\rm cm}^{-1}], \tag{3}$$

where τ_c is the Coulomb collisional optical depth, $\kappa(s)$ is the collisional damping rate of the radio wave, s [cm] is the distance along the ray path, and μ_r is the refraction index. For a fully ionized plasma with solar abundances $\sum_i Z_i^2 N_i = 1.16 N_e$. $\ln\Lambda_t$ is the Gaunt factor. T [K] is the thermal temperature. f_s ($\gtrsim f_{\rm pe}$) is the frequency of the wave from the source in units of Hz.

Here we consider that the wave generated in the corona is propagating upwards, and for simplicity, we also use one-dimensional (1D) wave propagation. The refraction index in the plasma is

$$\mu_r = \frac{v_g}{c} = \sqrt{1 - \frac{f_{\rm pe}^2}{f_s^2}}, \tag{4}$$

where v_g is the wave group speed, c is the speed of light in vacuum. Thus, for the wave of a given frequency f_s, which is excited at the height h_0 where $f_s \approx f_{\rm pe}(h_0)$, the collisional optical depth can be rewritten as:

$$\tau_c = \int_{h_0}^{\rm inf} \kappa_0 f_s^2 \frac{f_{\rm pe}^4}{f_s^4} \frac{1}{\sqrt{1 - \frac{f_{\rm pe}^2}{f_s^2}}} dh, \tag{5}$$

where κ_0 is a constant expressed as

$$\kappa_0 = 1.76 \times 10^{-18} \left(\frac{\ln\Lambda_t}{T^{3/2}} \right) [{\rm cm}^{-1}\,{\rm Hz}^{-2}]. \tag{6}$$

Though the integrand in Equation (5) is singular at $f_{\rm pe} = f_s$, the integration can be performed. In addition, the integral decreases quickly with the decrease of the frequency ratio $f_{\rm pe}/f_s$. This indicates that the main contribution of τ_c comes from the plasma near the radio source region with $f_{\rm pe} \lesssim f_s$, since the corona electron density is generally decreasing with the increase of altitude. As approved in Appendix A, the optical depth is determined mainly by the function of $f_{\rm pe}$ near the emitting region and is inversely proportional to the local decreasing rate of the background plasma frequency near the radio source region, namely,

$$\tau_c(f_s) \propto \left(-\frac{df_{\rm pe}}{dh}\bigg|_{f_{\rm pe}=f_s} \right)^{-1}. \tag{7}$$

Equation (7) indicates that, when the decreasing rate of plasma frequency locally (or the frequency drift rate according to Equation (1)) is large, the optical depth of the corresponding radio wave is relatively small, and the wave is less absorbed. If there is wavelike variation of the local corona density with altitude, one would observe similar variation of the frequency drift rate and flux intensity with the radio frequency. Therefore, Equations (1) and (7) can qualitatively explain the reason why the segments with larger absolute value of frequency drift rate tend to be brighter in the dynamic spectrum. While some assumptions were made for the derivation of Equation (7), it can qualitatively show the trend. In the following subsection, we present the numerical integration results based on a corona density model with fluctuation.

3.2. Numerical Calculation

For a given background electron density distribution $N_e(h)$, the frequency drift line $f(t)$ and the relative flux intensity of the wave can be obtained by numerically integrating Equation (1) and Equation (5), respectively. In the calculation we made several assumptions:

1. We assume 1D wave propagation along the line of sight.
2. The S-burst is generated by an electron beam propagating outward in the corona, exciting the wave at the local plasma frequency ($f_{\rm pe}$), and the wave starts to propagate along the radial direction.
3. The corona electron density can be described as

$$N_e(r) = N_{e0}(r) + \Delta N_e(r), \tag{8}$$

where the background density N_{e0} is chosen to be four times the density model of Saito et al. (1977),

$$N_{e0}(r) = 4 \left(\frac{1.36 \times 10^6}{r^{2.14}} + \frac{1.68 \times 10^8}{r^{6.13}} \right) [{\rm cm}^{-3}].$$

Here the heliocentric distance r is in units of solar radius.

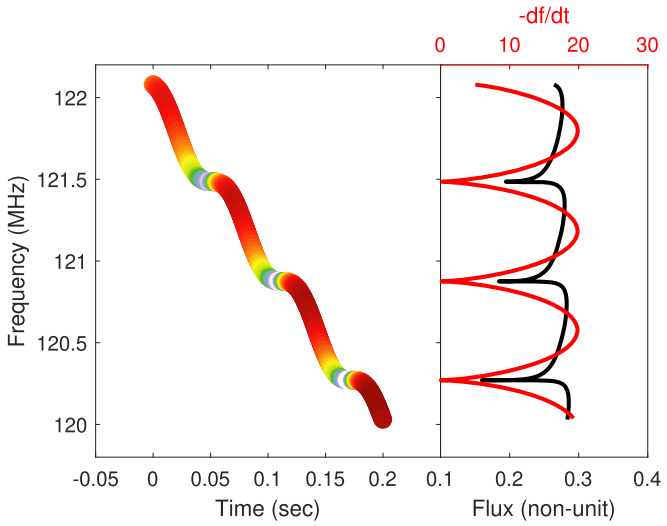

Figure 6. Simulated frequency drift line and the flux intensity, the color in the left subpanel indicates the relative intensity. In the right subpanel, the red line shows the frequency drift rate of this Sb-burst for different frequency, the black line shows the relative intensity calculated with Equations (2) and (5). The electron beam speed is set to 0.08 c in the simulation.

The disturbed electron density is expressed as

$$\Delta N_e(r) = \Delta N_{e0} \sin(2\pi r/\lambda),$$

where $\Delta N_{e0} = 2.85 \times 10^5$ cm^{-3} is the amplitude of the density fluctuation, $2\pi/\lambda = 3000$ corresponds to a wavelength of about 1.5 Mm.

4. The intensity of the wave generated by the beam does not vary drastically during the burst.
5. The wave is absorbed by Coulomb collisions during its propagation according to Equation (2).

With these assumptions, when the electron beam passes through the perturbed plasma, it will experience quasiperiodic changes in the density gradient, which corresponds to the wavy structure in the frequency drift of the burst. We calculated the optical depth τ_c between the generation site and the observer for the wave of different frequencies using Equation (5). The integration range is from the position with local plasma frequency of $f_{\rm pe} = (1 - 10^{-7})f_s$ to 200 solar radii. The relative flux intensity is calculated using Equation (2), then we overlap the relative intensity to the frequency drift line to simulate the dynamic spectrum of an S-burst with fine structure. The simulated dynamic spectrum is shown in Figure 6, from which we can see that it can reproduce the wavy frequency drift line and the segmented intensity distribution similar to our observation. The numerical calculation[10] is performed using the integral procedure in MATLAB, where the various step lengths are arranged by the procedure to achieve the optimal precision (Shampine 2008).

4. Conclusion and Discussion

In this work, we find 204 S-bursts within the 12 hr observations in the frequency range of 120–180 MHz of LOFAR on 2019 April 13. The frequency drift rate of the events is in good accordance with the previous results obtained in low frequency range (McConnell 1982; Dorovskyy et al. 2017; Morosan & Gallagher 2017; Clarke et al. 2019). Some of these 204 S-bursts have a clear substructure in the intensity and frequency drift rate. We proposed a theory to interpret the substructures of the Sb-bursts and the positive relationship between the drift rate df/dt and flux intensity $I_{\rm obs}$. With this theory, we can numerically reproduce the observed phenomena in the dynamic spectrum as shown in Figure 6. We also find the existence of the multilane structure in some of the S-burst, which may indicate the recurrent injection of the electron beams. For now, we are not able to give a theoretical explanation for the generation of drift pair. Future investigations concerning the drift pair's S-bursts with high time resolution radio imaging could help us understand the generation process of the multilanes seen in S-bursts.

According to the simulation, the wavy structure and the flux intensity variation of the Sb-burst can be recreated with the density fluctuations of background electron density at a length scale of about 1.5 Mm. The length scale of the density fluctuations determines the length of the "segments" in the Sb-burst substructures, the amplitude of $\Delta N_{e0}/N_{e0}$ determines how wavy the frequency drift line is, and the amplitude of the flux intensity variation. The simulation indicates that $\Delta N_{e0}/N_{e0} = 0.15\%$ is enough to produce the segmented fine structures. Larger amplitude of density fluctuation may result in positive $df_{\rm pe}/dh$. When there is positive $df_{\rm pe}/dh$, some of the wave can be reflected back and forth (or even become trapped) in the density well. As a result, these waves experience very strong collision absorption, and the corresponding S-Burst would have some discontinuity gaps with nearly zero flux in the dynamic spectrum.

From the intensity distribution of the observed Sb-burst, apart from the variation between segments, we can also see that it is modulated with smaller scale and amplitude variations. The smaller scale and amplitude variation in flux intensity may result from smaller scale and amplitude density variation in the coronal electron densities. Previous remote sensing observations (Mugundhan et al. 2017) show that the $\Delta N_{e0}/N_{e0}$ varies from 0.01 to 0.1 within 1.5 to 200 solar radii. The simulation of the frequency fine structure of type III radio bursts (Li et al. 2012) used 5% of $\Delta N_{e0}/N_{e0}$ at length scales of 15 Mm and produced comparable structure with the observation. There is still no density fluctuation model from in situ observations of the inner corona (<15 solar radii), and the recent *Parker Solar Probe* mission (Fox et al. 2016) will go as close as nine solar radii, which will constrain the estimation of the amplitude and the length scale of the coronal density fluctuations.

In the numerical calculation of optical depth (in Figure 6), we assumed an observed frequency near fundamental plasma frequency for the wave generation, which means, the wave comes from regions where $f_{\rm pe} \approx f_s$. This assumption was previously used in the numerical simulation of solar type III bursts (Takakura 1982; Li et al. 2008). Previous studies (McConnell 1983; Melnik et al. 2010; Morosan et al. 2015) also support the idea that the S-burst waves come from a region close to the local plasma frequency. To test the sensitivity of the flux intensity variation to the starting frequency of the wave, we changed the starting frequency of the wave propagation. For the result in Figure 6, the integration range of Equation (7) is from $h_0|_{f_{pe0}=(1-10^{-7})f_s}$ to 200 solar radii. We considered two more cases, the starting height of the wave propagation is changed to $h_0|_{f_{pe0}=0.5f_s}$ and $h_0|_{f_{pe0}=0.99f_s}$, the results are shown in Figure 7. From Figure 7, we can see that, if the wave comes from the region of the local plasma frequency

[10] The source code is available at an online repository (https://github.com/Pjer-zhang/SBurst-Numerical).

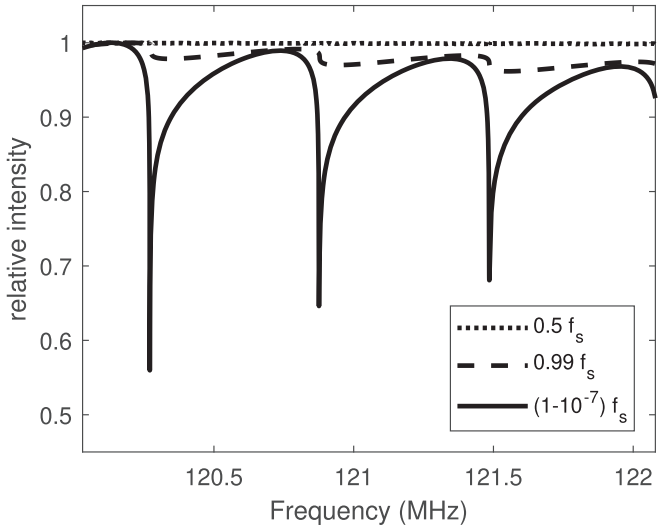

Figure 7. Flux intensity variation of the S-burst with different starting local plasma frequency.

(solid line in Figure 7), the variation in relative intensity is large. While, if the starting frequency is slightly away from the local plasma frequency, the variation of the flux intensity is smaller. For the harmonic wave, the calculated intensity variation is less than 10^{-4}. This indicates that the discontinuous fine structure is more likely to exist in the fundamental wave, not second or third harmonic ($2f_{\rm pe} = f_s$ or $3f_{\rm pe} = f_s$). The significant intensity variation of the Sb-burst requires not only density fluctuations, but also that, the wave is generated at the place of fundamental local plasma frequency.

In our computation, we do not consider the temporal variation and propagation of the density fluctuations. This assumption is proposed due to the relative timescale of the fluctuation variation and the electron beam motion. The S-bursts duration is much shorter than the timescale of the background density fluctuation variation with large length scales. The speed of the electron exciter is set as $0.08\,c$, which is much larger than the Alfvén speed in the corona. Moreover, density fluctuations can cause scattering of the radio waves during propagation, which is also not included in the simulation. The duration of the radio emission at a given frequency can also be broadened by scattering (Kontar et al. 2019). The increase of the duration may mix the segments of the discontinuity and weaken the significance of fine structures.

Finally, we would like to note that the variation of the flux intensity due to collisional absorption is independent on the emission mechanism of S-bursts, though plasma emission is emphasized in the above discussion. If the radio wave is considered to be generated by ECM in a density-depleted magnetic flux tube (Wu et al. 2002), the wave will be confined in the tube and propagate upwards before the local plasma frequency outside of the tube is equal to the wave frequency. If there are electron density fluctuations of the background corona outside of the magnetic tube, the variation of the flux intensity due to collisional absorption may also occur when the radio wave leaves the magnetic tube (or the apparent source region). The lower the density gradient is, the higher the absorption is, and vice versa. Moreover, from Equation (4), the wave propagation speed is lower when the local plasma frequency is closer to the wave frequency. When the density gradient is lower, the wave will leave the apparent source region with a lower speed, and as a result, the frequency drift rate df/dt is reduced. This is consistent with the above observation that the segments of S-burst with larger absolute value of frequency drift rate tend to be brighter in the dynamic spectrum. In the future, further imaging spectroscopy of the Sb-burst, especially polarization and imaging observations combined with the magnetic field topology can help interpret the emission mechanism of S-bursts.

We are thankful to the ASTRON/JIVE Summer Student Programme 2019 for the financial support. This paper is based on data obtained with the International LOFAR Telescope (ILT) under project code LT10 002. LOFAR (van Haarlem et al. 2013) is the Low Frequency Array designed and constructed by ASTRON. It has observing, data processing, and data storage facilities in several countries that are owned by various parties (each with their own funding sources) and that are collectively operated by the ILT foundation under a joint scientific policy. The ILT resources have benefited from the following recent major funding sources: CNRS-INSU, Observatoire de Paris and Universite Orleans, France; BMBF, MIWF- NRW, MPG, Germany; Science Foundation Ireland (SFI), Department of Business, Enterprise and Innovation (DBEI), Ireland; NWO, The Netherlands; The Science and Technology Facilities Council, UK; Ministry of Science and Higher Education, Poland. We also acknowledge Clarke for providing the data point of the frequency drift rate in low frequency. The research in USTC was supported by the National Nature Science Foundation of China (41574167 and 41974199).

Appendix A
Qualitative Analysis of Coulomb Absorption

Consider the integration of Equation (5) from h_0 where $f_{\rm pe} = f_s$ to infinitely far away ($f_{\rm pe} = 0$), the optical depth can be rewritten as

$$\tau_c = \int_{h_0}^{\rm inf} \kappa_0 f_s^2 \frac{f_{\rm pe}^4}{f_s^4} \frac{1}{\sqrt{1-\frac{f_{\rm pe}^2}{f_s^2}}} dh = \int_{f_s}^{0} \kappa_0 f_s^2 \frac{f_{\rm pe}^4}{f_s^4} \frac{1}{\sqrt{1-\frac{f_{\rm pe}^2}{f_s^2}}} \frac{1}{\frac{df_{\rm pe}}{dh}} df_{\rm pe}, \quad (9)$$

where $f_{\rm pe} \leqslant f_s$ is required. For a given radio frequency f_s, the integrand decreases sharply with the decrease of the frequency ratio $f_{\rm pe}/f_s$, roughly in the order of $(f_{\rm pe}/f_s)^4$. In general, the electron density and the plasma frequency decrease with the altitude in corona, so the main contribution of τ_c comes from the plasma in a limited region near the radio source position with $f_{\rm pe} \lesssim f_s$. As an result, the gradient $df_{\rm pe}/dh$ can be taken out of the integration with the approximation $(df_{\rm pe}/dh) \sim (df_{\rm pe}/dh)|_{f_{\rm pe}=f_s}$.

After applying the element changing of $u := f_{\rm pe}/f_s$, the integration can be simplified into (Gradshteyn & Ryzhik 2014)

$$\tau_c = \kappa_0 f_s^3 \left(-\frac{df_{\rm pe}}{dh}\bigg|_{f_{\rm pe}=f_s} \right)^{-1} \int_0^1 u^4 \frac{1}{\sqrt{1-u^2}} du \quad (10)$$

$$=\kappa_0 f_s^3 \left(-\frac{df_{\rm pe}}{dh}\bigg|_{f_{\rm pe}=f_s} \right)^{-1} \left(\frac{3\pi}{16}\right). \quad (11)$$

The integrand has a singular point at $f_{\rm pe} = f_s$ in Equation (9) or at $u = 1$ in Equation (10), but the integration is convergent. The optical depth is a finite value for the wave originates from the place where $f_{\rm pe} = f_s$. From Equation (11), we can see that the optical depth is inversely proportional to the local plasma frequency decreasing rate,

$$\tau_c \propto \left(-\frac{df_{\rm pe}}{dh}\bigg|_{f_{\rm pe}=f_s} \right)^{-1}. \quad (12)$$

In other words, the optical depth τ_c is determined mainly by the function $f_{\rm pe}(h)$ near the emitting region. This is consistent with the numerical integration result shown in Figure 6.

We need to note that negative value of $df_{\rm pe}/dh$ is assumed in above discussion. When the density fluctuation is strong enough to create a positive $df_{\rm pe}/dh$ in the decreasing background, the wave generated at $f_{\rm pe} = f_s$ cannot propagate toward the observer in this one-dimensional model. Consequently, the corresponding radio source is not visible to the observer.

Appendix B
Convergence of the Numerical Integration

Although the integration in Equations (5) and (9) is convergent theoretically, the numerical integrating result is sensitive to the starting point near the singularity as shown in Figure 8. We can see that the minimum of the relative flux converges when the local plasma frequency of the starting point approaches the frequency of the wave as $(f_s - f_{\rm pe0})/f_s \to 0$.

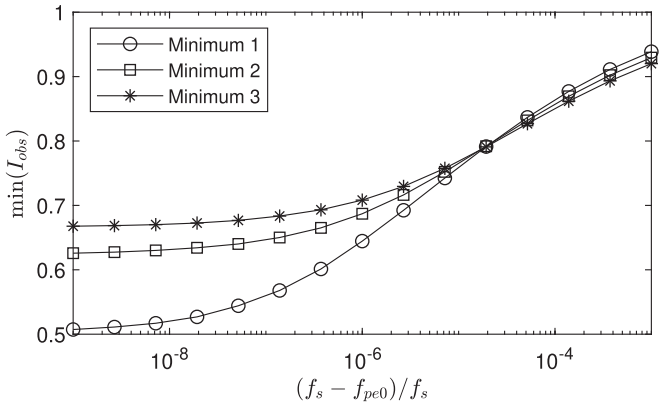

Figure 8. Minimum value of the relative flux with different local starting frequency $f_{\rm pe0}$. Here, the minimum 1, 2, and 3 represent the minimal points near the frequency 120.2 MHz, 120.9 MHz, 121.5 MHz on the black line in the left subpanel of Figure 6, respectively.

ORCID iDs

PeiJin Zhang https://orcid.org/0000-0001-6855-5799
Pietro Zucca https://orcid.org/0000-0002-6760-797X
ChuanBing Wang https://orcid.org/0000-0001-6252-5580
Mario M. Bisi https://orcid.org/0000-0001-6821-9576
Jasmina Magdalenic https://orcid.org/0000-0003-1169-3722
Christian Vocks https://orcid.org/0000-0001-8583-8619

References

Benz, A. O. 2012, Plasma Astrophysics: Kinetic Processes in Solar and Stellar Coronae (Dordrecht: Springer)
Chen, X., Kontar, E. P., Yu, S., et al. 2018, ApJ, 856, 73
Clarke, B. P., Morosan, D. E., Gallagher, P. T., et al. 2019, A&A, 622, A204
Dorovskyy, V., Melnik, V., Konovalenko, A., et al. 2017, in Proc. of the 8th Int. Workshop on Planetary, Solar and Heliospheric Radio Emissions, ed. G. Fischer et al. (Vienna: Austrian Academy of Sciences Press), 369
Ellis, G. 1969, AuJPh, 22, 177
Fox, N., Velli, M., Bale, S., et al. 2016, SSRv, 204, 7
Frisch, U., & Kolmogorov, A. N. 1995, Turbulence: The Legacy of AN Kolmogorov (Cambridge: Cambridge Univ. Press)
Gradshteyn, I. S., & Ryzhik, I. M. 2014, Table of Integrals, Series, and Products (New York: Academic)
Kolotkov, D. Y., Nakariakov, V. M., & Kontar, E. P. 2018, ApJ, 861, 33
Kontar, E. P., Chen, X., Chrysaphi, N., et al. 2019, ApJ, 884, 122
Li, B., Cairns, I. H., & Robinson, P. 2012, SoPh, 279, 173
Li, B., Cairns, I. H., & Robinson, P. A. 2008, JGRA, 113, A06104
Loi, S. T., Cairns, I. H., & Li, B. 2014, ApJ, 790, 67
Mann, G., Baumgaertel, K., Chernov, G., & Karlický, M. 1989, SoPh, 120, 383
McConnell, D. 1982, SoPh, 78, 253
McConnell, D. 1983, SoPh, 84, 361
McConnell, D., & Ellis, G. 1981, SoPh, 69, 161
Melnik, V., Konovalenko, A., Rucker, H., et al. 2010, SoPh, 264, 103
Melrose, D. 1982, in Solar Radio Storms, CESRA Workshop 4, ed. A. O. Benz & P. Zlobec, 182
Morosan, D., & Gallagher, P. 2017, Planetary Radio Emissions VIII (Vienna: Austrian Academy of Sciences Press), 357
Morosan, D., Gallagher, P., Zucca, P., et al. 2015, A&A, 580, A65
Morosan, D., Zucca, P., Bloomfield, D., & Gallagher, P. 2016, A&A, 589, L8
Mugundhan, V., Hariharan, K., & Ramesh, R. 2017, SoPh, 292, 155
Saito, K., Poland, A. I., & Munro, R. H. 1977, SoPh, 55, 121
Shampine, L. F. 2008, JCoAM, 211, 131
Stanislavsky, A., Volvach, Y., Konovalenko, A., & Koval, A. 2017, SunGe, 12, 99
Takakura, T. 1982, SoPh, 78, 141
Wang, C. B. 2015, ApJ, 806, 34
van Haarlem, M. á., Wise, M., Gunst, A., et al. 2013, A&A, 556, A2
Woo, R. 1996, Natur, 379, 321
Wu, C. S., & Lee, L. C. 1979, ApJ, 230, 621
Wu, C. S., Wang, C. B., Yoon, P. H., Zheng, H. N., & Wang, S. 2002, ApJ, 575, 1094
Zhang, P., Wang, C. B., & Ye, L. 2018, A&A, 618, A165